# Position Control of Parallel-Plate Microactuators for Probe-Based Data Storage

Michael S.-C. Lu and Gary K. Fedder, *Senior Member, IEEE*

*Abstract*—In this paper, we present the use of closed-loop voltage control to extend the travel range of a parallel-plate electrostatic microactuator beyond the pull-in limit. Controller design considers nonlinearities from both the parallel-plate actuator and the capacitive position sensor to ensure robust stability within the feedback loop. Desired transient response is achieved by a pre-filter added in front of the feedback loop to shape the input command. The microactuator is characterized by static and dynamic measurements, with a spring constant of 0.17 N/m, mechanical resonant frequency of 12.4 kHz, and effective damping ratio from 0.55 to 0.35 for gaps between 2.3 to 2.65 $\mu$m. The minimum input-referred noise capacitance change is 0.5 aF$/\sqrt{\text{Hz}}$ measured at a gap of 5.7 $\mu$m, corresponding to a minimum input-referred noise displacement of 0.33 nm$/\sqrt{\text{Hz}}$. Measured closed-loop step response illustrates a maximum travel distance up to 60% of the initial gap, surpassing the static pull-in limit of one-third of the gap. [1108]

*Index Terms*—Capacitive sensor, CMOS-MEMS, electrostatic pull-in, nonlinear plant, unstable pole.

## I. INTRODUCTION

FOR many years a well-known yet challenging problem for MEMS researchers interested in electrostatic actuation has been to extend the travel range of parallel-plate type electrostatic microactuators beyond the normal pull-in instability, which occurs at a displacement of one-third of the original gap. Several approaches have been proposed, including touch-mode actuators [1], [2], curved-electrode actuators [3], the leverage bending method [4], the series capacitor approach [5], charge control [6]–[9], and voltage feedback control [10], [11]. Motions of touch-mode actuators using dielectric-coated electrodes are difficult to control due to the stiction problem. The majority of them focus on increasing the pull-in limit by design of special actuator geometry; thereby the travel distance can be extended by open-loop operation. Geometric design changes are usually at cost of more driving voltage and/or larger design area than those of a conventional parallel-plate actuator design. For the charge-control approach using current drives, it is important to control the leakage current (on the order of pA) into the actuator in order to limit the injected charge. Experimental results of a stable travel distance up to 60% and 88% of the gap have been reported in [5] and [4], respectively.

Any physical object to be controlled in a closed-loop feedback system is called a plant. For our case, the plant is mainly the parallel-plate actuator, which is highly nonlinear and exhibits unstable behavior beyond the pull-in limit. The biggest challenge inherited by the voltage feedback control approach is to design and implement the closed-loop control system to stabilize the actuator in the unstable regime, and to achieve desired output response. The few studies in the past mainly focused on stability analysis and simulation [10], [11]. Closed-loop voltage control presented in this paper originates from development of a probe-based magnetic micro disk drive [12]. In the envisioned system, arrays of tip actuators are fabricated by a conventional CMOS process with integrated circuits for feedback control and data channels. Read/write probe heads located on actuators should be servoed up to 10 nm away from the top magnetic media for data read and write. Given an initial gap between 2 to 3 $\mu$m, and a tip height of 500 nm, the actuator displacement has to reach 75% to 83% of the gap for data access. In addition to stabilizing the actuator beyond the pull-in limit, the use of voltage feedback control here also achieves a desired output response in the presence of external disturbances and plant uncertainties, such as the initial gap variation.

A conventional controller design for given nonlinear plants is through the finding of a Lyapunov function [13] for stability analysis. However it is nontrivial to prove global asymptotic stability for lack of a general way to find an explicit Lyapunov function that leads to the controller design, and even successful identification of a Lyapunov function rarely leads to control laws that can be easily implemented by analog circuits [14]. For ease of implementation, we select design of a linear time-invariant (LTI) controller over a nonlinear or a linear time-varying (LTV) controller. Controller design is through linearization of the nonlinear plant, and stability analysis is performed in the frequency domain in order to optimize the phase margin at every operating point.

In Section II, the control system block diagram is first presented, followed by fabrication of microactuators using the CMOS-MEMS technology in Section III. Then modeling and design of the plant, including the parallel-plate tip actuator and the capacitive position sensor, are introduced in Section IV. Controller design is studied in Section V. Experimental results on plant characterization are illustrated in Section VI. In Section VII, we present measured closed-loop step responses, followed by conclusions in Section VIII.
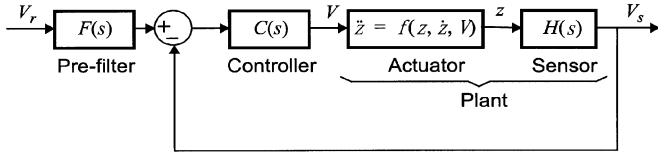
Fig. 1.   Two degree-of-freedom feedback system configuration.



Fig. 2.   Cross section of the CMOS-MEMS process flow. (a) After CMOS processing. (b) After anisotropic dielectric reactive-ion etch for definition of structural sidewalls. (c) After anisotropic silicon etch. (d) After isotropic silicon etch for structural release.

## II. BLOCK DIAGRAM

The control system block diagram illustrated in Fig. 1 has two transfer functions to be designed [15]. One is the controller, which achieves robust stability within the loop in the presence of the unstable pole and plant uncertainties, and the other is the pre-filter, which shapes the input command for the feedback loop to track and follow. Both the controller and pre-filter can be implemented by linear circuits as they are represented by Laplace transforms $C(s)$ and $F(s)$, respectively. The plant consists of the parallel-plate actuator represented by a nonlinear differential equation, and the capacitive position sensor represented by the Laplace transfer function $H(s)$, with a nonlinear gain dependent on the actuator displacement.

## III. DEVICE FABRICATION

Fabrication of devices starts with a commercial CMOS process (Austria Micro System (AMS) 0.5-$\mu$m three-metal two-poly CMOS), followed by post-CMOS micromachining steps described in [16]. First, an anisotropic dielectric reactive-ion etch (RIE) with $CHF_3/O_2$ plasma defines the structural sidewalls with the top metal layer used as an etch-resistant mask. The oxide etch rate is 424 Å/min. Next, a deep silicon reactive-ion etch is performed in an inductively coupled plasma at an etch rate of 2.9 $\mu$m/min. The etch uses the advanced silicon etch process [17] with alternating cycles of $SF_6/O_2$ plasma for etch and $C_4F_8$ for passivation. Finally, microstructures are released from the substrate by an isotropic silicon RIE at 1 $\mu$m/min. The complete process flow in cross section is depicted in Fig. 2.

## IV. PLANT MODELING AND DESIGN

The dynamic equation of a conventional parallel-plate microactuator shown schematically in Fig. 3 is given by

$$m\ddot{z} + b\dot{z} + kz = \frac{\varepsilon_o A}{2(g-z)^2}V^2 \qquad (1)$$

where $m$ is the mass, $b$ is the squeeze-film damping coefficient, $k$ is the spring constant, $\varepsilon_o$ is the permittivity of free space, $A$ is the parallel-plate area, $g$ is the initial gap separation, $z$ is the actuator displacement, and $V$ is the applied voltage. Nonlinearities arise from the electrostatic force, whose magnitude is proportional to applied voltage squared, and is displacement dependent. The squeeze-film damping force is time-varying, depending on the plate displacement and velocity. Total damping force can be simulated by a lumped-parameter model consisting of parallel branches of series-connected spring and damper elements [18]–[20]. The resulting time-varying damping coeffi-
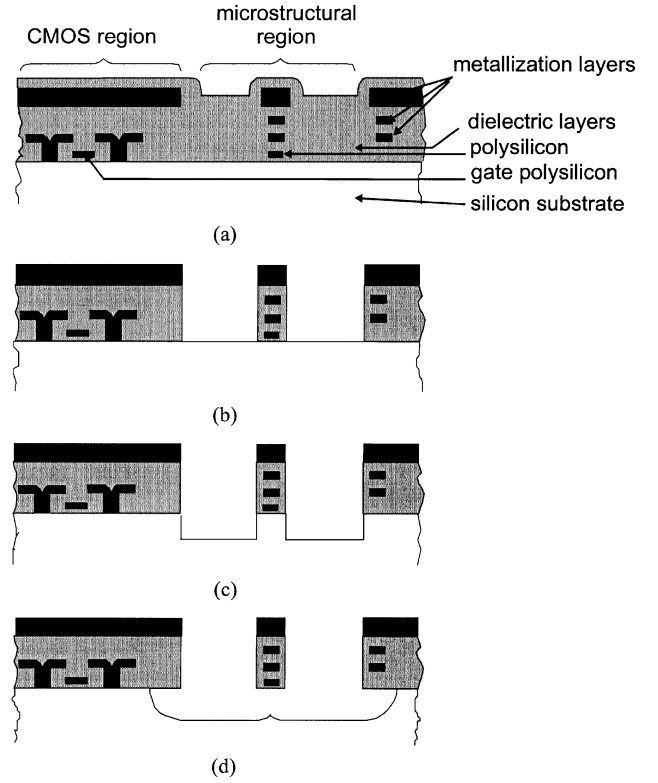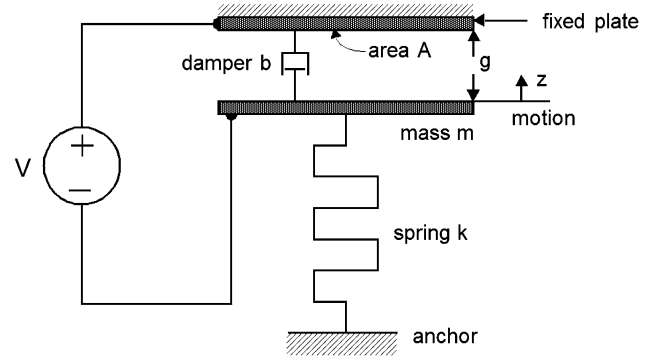


Fig. 3.   Schematic of a conventional parallel-plate microactuator.

cients at different displacements are collectively expressed by a range of values as $b \in [b_l, b_u]$.

With a small variation of $\Delta z$ and $\Delta v$ around the operating point $(Z_o, V_o)$, we can obtain the small-signal actuator dynamics by using Taylor's series expansion of the electrostatic force. By elimination of higher order terms, the linearized actuator dynamics are derived as:

$$m\Delta\ddot{z} + b\Delta\dot{z} + (k+k_e)\Delta z = \frac{2kZ_o}{V_o}\Delta v \qquad (2)$$

where

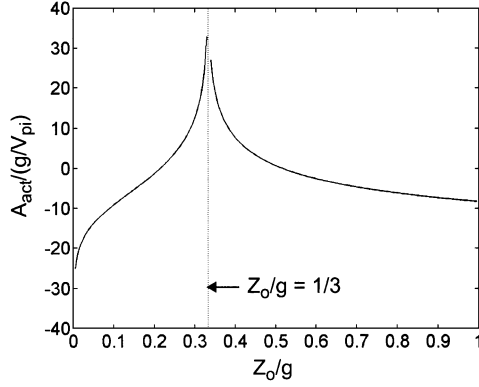$$k_e = -\left(\frac{2\alpha}{1-\alpha}\right)k \qquad (3)$$

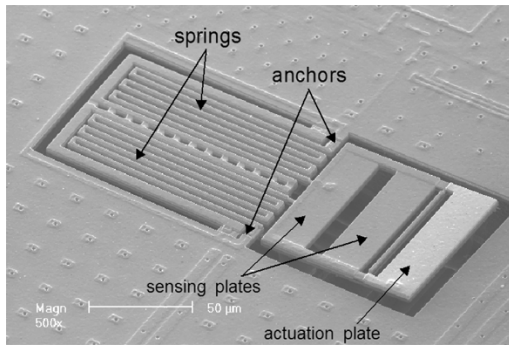Fig. 4. Normalized dc actuator gain as a function of normalized displacement.



Fig. 5. SEM of released microactuator fabricated by CMOS-MEMS process.

and $\alpha$ in (3) is the normalized displacement, $Z_o/g$, at operating point $Z_o$. The electrostatic force gradient induces a "negative" spring constant which is a function of plate displacement. As the ratio $\alpha$ becomes 1/3, the electrical spring constant completely negates the mechanical spring constant, thereby creating a pole frequency at zero. The actuator behaves like a "mechanical integrator" at this point, and becomes unstable as $\alpha$ increases beyond 1/3. Substituting $Z_o = g/3$ into (1) at steady state gives the pull-in voltage

$$V_{pi} = \sqrt{\frac{8kg^3}{27\varepsilon_o A}}. \tag{4}$$

The dc actuator gain in (2) can be further expressed as a function of normalized displacement by

$$A_{\mathrm{act}} = \left.\frac{\Delta z}{\Delta v}\right|_{\omega=0} = \frac{4\sqrt{3\alpha}}{9|1-3\alpha|} \cdot \frac{g}{V_{pi}}. \tag{5}$$

The normalized dc actuator gain as a function of normalized displacement is plotted in Fig. 4. The dc gain at one-third of the gap is infinity, therefore a large gain variation in that region is shown. This large gain variation can result in increase of servo bandwidth in order to obtain adequate stability margins [25].

A released microactuator is illustrated in Fig. 5. Two sensing plates and an actuation plate are mechanically connected but electrically isolated from each other. The space between plates ensures adequate silicon undercut during release etch, and

reduces the feedthrough capacitance between the actuation plate and the sensing plate. Each spring carries the actuation and sensed signals individually, and a grounded shielding is inserted in between signals when crossing is unavoidable. An external electrode is placed on top (not shown in the graph) of the actuator to form the initial gap and the actuated and sensing capacitances.

A schematic representation of the entire feedback control system is depicted in Fig. 6, which illustrates that capacitive position sensing is achieved through a single-ended capacitive bridge by modulation/amplification/demodulation, followed by low-pass filtering to remove the $1 \times$ and $2 \times$ carrier-frequency signals. An initial dc sensed voltage due to the single-ended sensing scheme has to be nulled before the closed-loop servo is turned on. The magnitude of the sensed output voltage is a function of actuation-plate displacement given by

$$|V_s| = A_v A_d |V_m|$$
$$\times \left(\frac{C_{s1}(z) + C_{s2}(z)}{C_{s1}(z) + C_{s2}(z) + C_i} - \frac{C_{s10} + C_{s20}}{C_{s10} + C_{s20} + C_i}\right) \tag{6}$$

where $A_v$ is the pre-amp gain, $A_d$ is the demodulator gain, $V_m$ is the modulation voltage, $C_{s1}$ and $C_{s2}$ are the sensing capacitances between the sensing plate 1 and sensing plate 2 to the top electrode, respectively, $C_{s10}$ and $C_{s20}$ are the initial sensing capacitances, and $C_i$ is the pre-amp input capacitance. The displacements of the sensing plates are obtained by finite-element simulation [21] with given actuation plate displacements $z$ to account for the cantilever rotation. Substituting the displacements into the sensing capacitances gives

$$C_{s1}(z) = \frac{\varepsilon_o A}{g - 0.84z}, \quad C_{s2}(z) = \frac{\varepsilon_o A}{g - 0.67z} \tag{7}$$

where the capacitance variation from the small angular tilt is not considered. The capacitive sensor gain at an operating point $z = Z_o$ is defined by differentiation of the sensed output with respect to the displacement. By including the dominant pole, $\omega_p$, from the low-pass filter, the sensor transfer function at $z = Z_o$ is,

$$H(s)|_{z=Z_o} = \frac{\left(\frac{dV_s}{dz}\right)_{z=Z_o}}{1 + \frac{s}{\omega_p}} = \frac{G(Z_o)}{1 + \frac{s}{\omega_p}}. \tag{8}$$

The sensing pre-amplifier shown schematically in Fig. 7(a) is a noninverting amplifier with the core implemented by a high-gain folded-cascode op-amp as shown in Fig. 7(b). The designed op-amp has a high gain-bandwidth product around 60 MHz in order to raise the selected modulation frequency, and also the cutoff frequency of the low-pass filter. Therefore the phase lag within the feedback loop is reduced, which is important for control of an unstable plant. The dc open-loop gain of the op-amp is close to 100 dB, and the closed-loop gain of the pre-amp is set at 10 by ratioed polysilicon resistors in CMOS ($R_{\mathrm{poly}} = 33\,\Omega/\mathrm{sq.}$). DC bias at the pre-amp input node is provided through a large resistance implemented by a transistor operated in the sub-threshold regime. Demodulation is currently realized by a commercial double-balanced demodulator chip
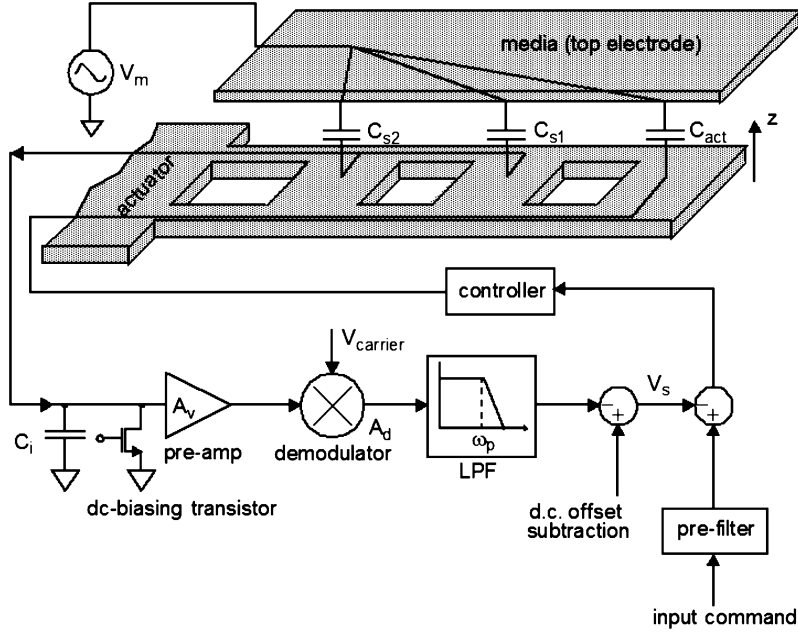
Fig. 6.   Schematic representation of feedback control system around parallel-plate microactuator. Routing for sensing and actuation signals uses separate interconnect layers for electrical isolation.

(LM 1496), the so-called Gilbert cell [22], with a voltage conversion gain of 5.

Plant parameters used for controller design are: $m = 3 \times 10^{-11}$ kg, $k = 0.167$ N/m, $C_i = 408$ fF, $A_v = 10$, $A_d = 5$, $A = 1600$ $\mu$m$^2$, $g = 3$ $\mu$m, and $\omega_p = 120$ kHz. The squeeze-film damping ratio, $\xi = b/(2\sqrt{km})$, is computed between 0.4 to 240 for gaps from 3 $\mu$m to 0.2 $\mu$m by NODAS simulation [23] as shown in Fig. 8.

## V. CONTROLLER DESIGN

The desired response time of the actuator under servo is in the ms range. It is reasonable to assume that the motion is quasi-static, because the designed actuator bandwidth (11.9 kHz), when fully utilized, is capable of achieving submilliseconds response time. Therefore the controller design can be realized through linearization of the nonlinear plant, since it behaves similarly to its linearized approximation at each point along the motion trajectory. Local stability is analyzed by the frequency-domain method using phase margin and gain margin. By design of the prefilter to shape the input step command, the actuator position is controlled quasi-statically along the motion trajectory. The effects of initial conditions and high-order terms of electrostatic force omitted during linearization can be considered additionally as an input-disturbance rejection problem [24] to extend from local stability to global stability. The linearized actuator has one unstable pole for displacements beyond the pull-in limit. Magnitude of the unstable pole frequency increases with respect to the increased displacement. The cost of feedback for given unstable plants is the increase of open-loop bandwidth in order to maintain adequate stability margins, and to avoid a large peak in the closed-loop frequency response. A rule of thumb states that the open-loop crossover frequency should be at least twice as large as the unstable pole

frequency to give a 60° phase margin [25] and a peak value less than 4 dB [26].

Combining the transfer functions of the linearized actuator in (2) and the capacitive sensor in (8) gives the linearized plant at operating point $(Z_o, V_o)$

$$P(s) = \frac{G(Z_o) \cdot \left( \frac{2kZ_o}{V_o} \right)}{\left( 1 + \frac{s}{\omega_p} \right) \left( ms^2 + bs + \left( \frac{1-3\alpha}{1-\alpha} \right) k \right)}. \quad (9)$$

Rewriting (9) using the resonant frequency $\omega_n = \sqrt{k/m}$ and the damping ratio, and multiplying the plant with a proportional-gain controller $C(s) = k_p$ gives the open-loop transfer function in the unstable regime

$$L(s) = \frac{K}{\left( 1 + \frac{s}{\omega_p} \right) (s^2 + 2\xi_e \omega_e s - \omega_e^2)} \quad (10)$$

where

$$K = k_p G(Z_o) \left( \frac{2Z_o}{V_o} \right) \omega_n^2 \quad (11)$$

and the effective resonant frequency and the effective damping ratio due to the electrical spring-softening effect are

$$\omega_e = \sqrt{\frac{3\alpha - 1}{1 - \alpha}} \omega_n, \quad \xi_e = \sqrt{\frac{1 - \alpha}{3\alpha - 1}} \xi. \quad (12)$$

The magnitude and phase of $L(j\omega)$ are given by

$$|L(j\omega)| = \frac{K}{\sqrt{1 + \frac{\omega^2}{\omega_p^2}} \sqrt{(\omega^2 + \omega_e^2)^2 + (2\xi_e \omega_e \omega)^2}} \quad (13)$$
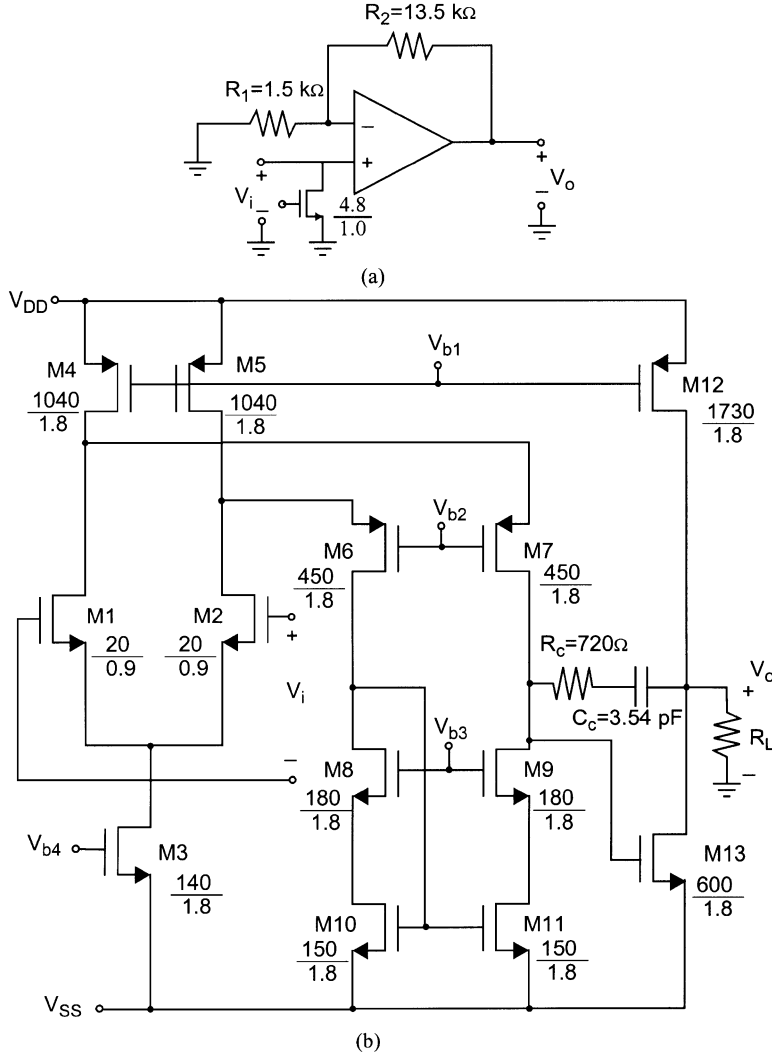
Fig. 7. (a) Schematic of sensing pre-amp in a noninverting amplifier configuration. (b) Schematic of folded-cascode operational amplifier with a common-source amplifier as the output stage. The units of the transistor widths and lengths are in micrometers.
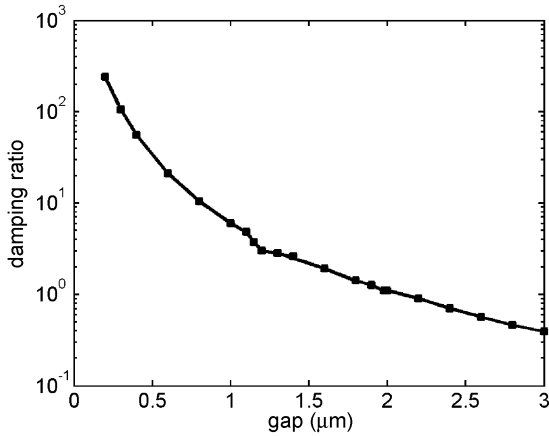


Fig. 8. Squeezed-film damping ratio of parallel-plate actuator versus gap separation at atmospheric pressure.

and

$$\angle L(j\omega) = -\pi + \tan^{-1}\left(\frac{2\xi_e \omega_e \omega}{\omega^2 + \omega_e^2}\right) - \tan^{-1}\left(\frac{\omega}{\omega_p}\right). \quad (14)$$

Substituting the phase margin $\phi$, and the crossover frequency $\omega = \omega_\phi$ into (14) gives

$$\phi = \tan^{-1}\left(\frac{\frac{2\xi_e \omega_e \omega_\phi}{\omega_\phi^2 + \omega_e^2} - \frac{\omega_\phi}{\omega_p}}{1 + \frac{2\xi_e \omega_e \omega_\phi}{\omega_\phi^2 + \omega_e^2} \cdot \frac{\omega_\phi}{\omega_p}}\right). \quad (15)$$

Equating $\angle L(j\omega)$ to $-\pi$ at the upper gain-margin frequency yields

$$\omega_g = \sqrt{\omega_e(2\xi_e \omega_p - \omega_e)}. \quad (16)$$

Then substituting (16) into (13) gives the upper gain margin

$$G_H = \left[\frac{K}{2\xi_e \omega_e \omega_p \left(1 + \frac{2\xi_e \omega_e}{\omega_p} - \frac{\omega_e^2}{\omega_p^2}\right)}\right]^{-1}. \quad (17)$$
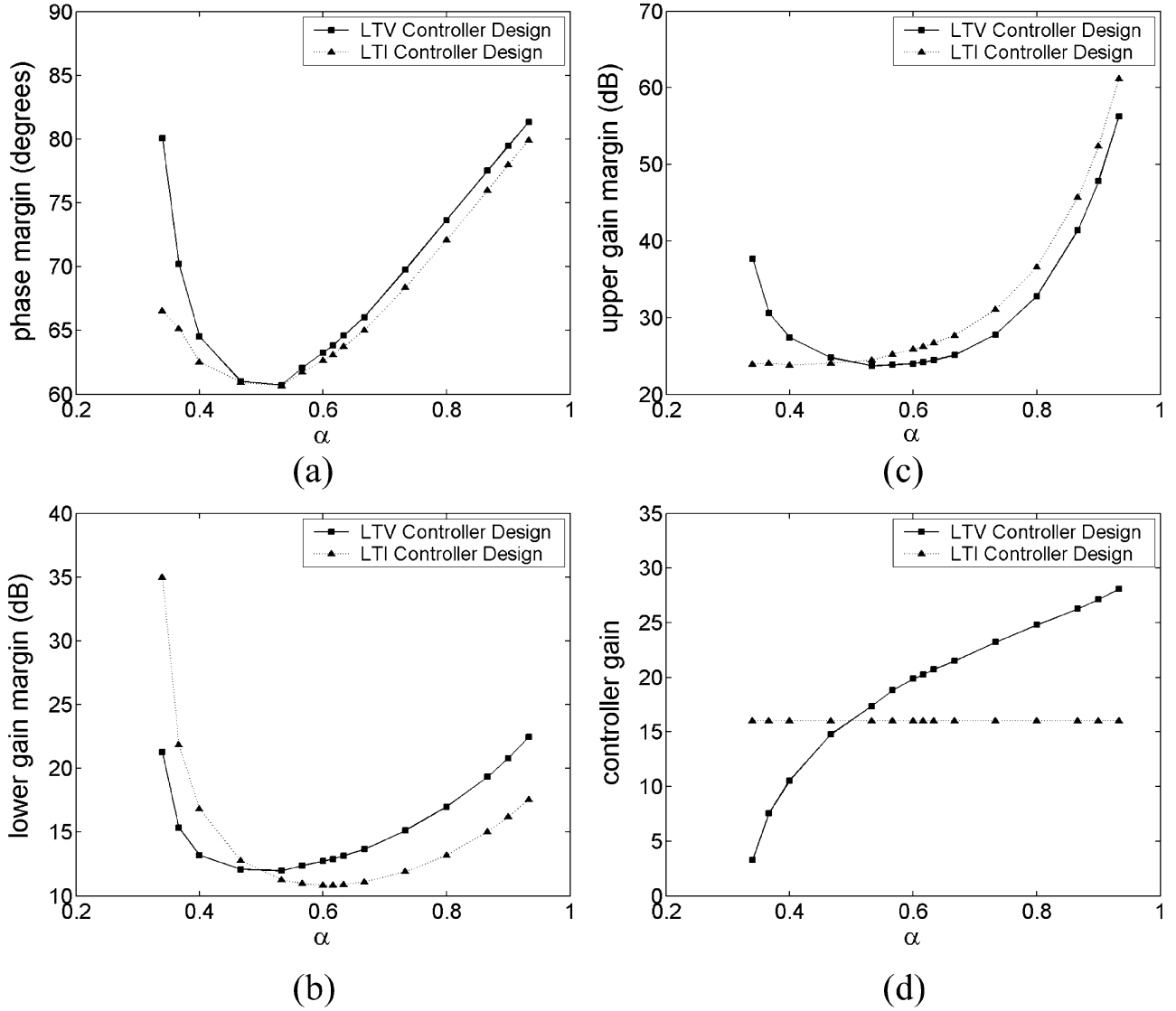
Fig. 9.   Maximum phase margin, and corresponding lower gain margin, upper gain margin, and controller gain as a function of normalized displacement from (a) to (d). Selected controller is $k_p = 16$, which gives a minimum phase margin around $60°$ at all displacements.

Equating $|L(j\omega)|$ to one at $\omega = \omega_\phi$ yields

$$K = \frac{\sqrt{\omega_\phi^2 + \omega_p^2}\sqrt{\left(\omega_\phi^2 + \omega_e^2\right)^2 + (2\xi_e\omega_e\omega_\phi)^2}}{\omega_p}. \quad (18)$$

By replacing $\omega = 0$ and (18) into (13), the lower gain margin is given by

$$G_L = \sqrt{1 + \left(\frac{\omega_\phi}{\omega_p}\right)^2}\sqrt{\left(1 + \left(\frac{\omega_\phi}{\omega_e}\right)^2\right)^2 + \left(\frac{2\xi_e\omega_\phi}{\omega_e}\right)^2}. \quad (19)$$

With one unstable pole in $L(s)$, closed-loop stability is achieved using the Nyquist stability criterion [27] with one encirclement around the $-1 + j0$ point on the complex plane. $\angle L(j\omega)$ starts from $-180°$ at $\omega = 0$ to $-270°$ at $\omega = \infty$. To find the maximum phase margin, $\angle L(j\omega)$ is differentiated with respect to $\omega$ at $\omega = \omega_\phi$. The resultant crossover frequency with

maximum phase margin is the solution of the following quartic equation:

$$(\omega_p + 2\xi_e\omega_e)\omega_\phi^4 + \left(2\xi_e\omega_p^2\omega_e + 2\omega_p\omega_e^2 + 4\xi_e^2\omega_p\omega_e^2 - 2\xi_e\omega_e^3\right)$$
$$\cdot\omega_\phi^2 - \left(2\xi_e\omega_p^2\omega_e^3 - \omega_p\omega_e^4\right) = 0. \quad (20)$$

Given calculated values of $\omega_p/\omega_e$ and $\xi_e$ according to the ratio $\alpha$, $\omega_\phi$ is first solved from (20). Then the maximum phase margin, and the corresponding lower gain margin, upper gain margin, and controller $k_p$ are computed by (15), (19), (17), and (11). Using the plant parameters given in Section IV, we plot the calculated values from Fig. 9(a)–(d). The phase margin at large displacements is over $60°$ due to the large damping ratios at small gaps. The optimal controller gain which gives the maximum phase margin varies with the displacement, implying that the optimal controller should be linear time-varying (LTV) in order to secure the largest phase margin at all displacements. A suboptimal linear time-invariant (LTI) controller, $k_p = 16$, is selected for implementation, and it gives a least phase margin
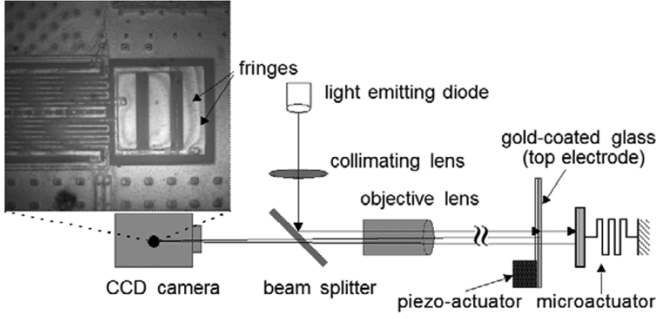
Fig. 10. Schematic of custom interferometric setup.

of around $60°$ at each displacement as shown in Fig. 9(a). The resultant gain margins are illustrated in Fig. 9(b) and (c).

The controller design also has to ensure stability for operating points less than one-third of the gap, where the actuator is stable. Our stability analysis [24] shows that the controller gain $k_p$ can be as large as 1000 before the system is destabilized. Therefore the selected gain $k_p = 16$ can guarantee system stability before and after the pull-in limit.

Tracking speed of the output response is determined by the pre-filter design. For quasi-static operation, cut-off frequency of the pre-filter can be less than 5% of the microactuator resonant frequency, and the required driving voltage is close to the actuator pull-in voltage (less than 15 V). For fast operation utilizing the full actuator bandwidth, the required driving voltage is approximately five times of the pull-in voltage [24]. For the intended microdisk drive application, position servo with a rise time (0 to 100% of the final value) less than 3 ms is sufficient, resulting in a prefilter design given by

$$F(s) = \frac{1}{1 + \frac{s}{1800}}. \tag{21}$$

## VI. PLANT CHARACTERIZATION

A custom micropositioning assembly with interferometric measuring capability was built to set up the initial gap between parallel plates. The electrode placed on top of the actuator was a slender glass substrate coated with a thin conductive gold layer. A piezoactuator was attached to the glass piece for fine control of initial gap separation. The fringe patterns were formed by light beams reflected from the gold layer and the actuator, with the image being collected by a charge-coupled-device (CCD) camera, as illustrated by the schematic representation in Fig. 10. An orange/red light-emitting diode (LED) ($\lambda = 635$ nm) was used as the light source. Each fringe occurs at multiples of a half wavelength of the LED.

Sensing and actuated capacitances were affected by structural curl of the actuator. Curl was measured using the WYCO NT3300 white-light interferometer. We obtained an actuation plate tilt of $2.9°$, and $2°$ and $2.9°$ for the two sensing plates. Capacitance models which consider plate tilt and fringing field lines were established by least-squares fit of data obtained from finite-element simulations [28].

To measure the $z$-directional spring constant and the pre-amp input capacitance, we performed a series of static displacement-voltage measurements at various initial gaps using capacitive sensing. Plate displacement was determined by the fringe
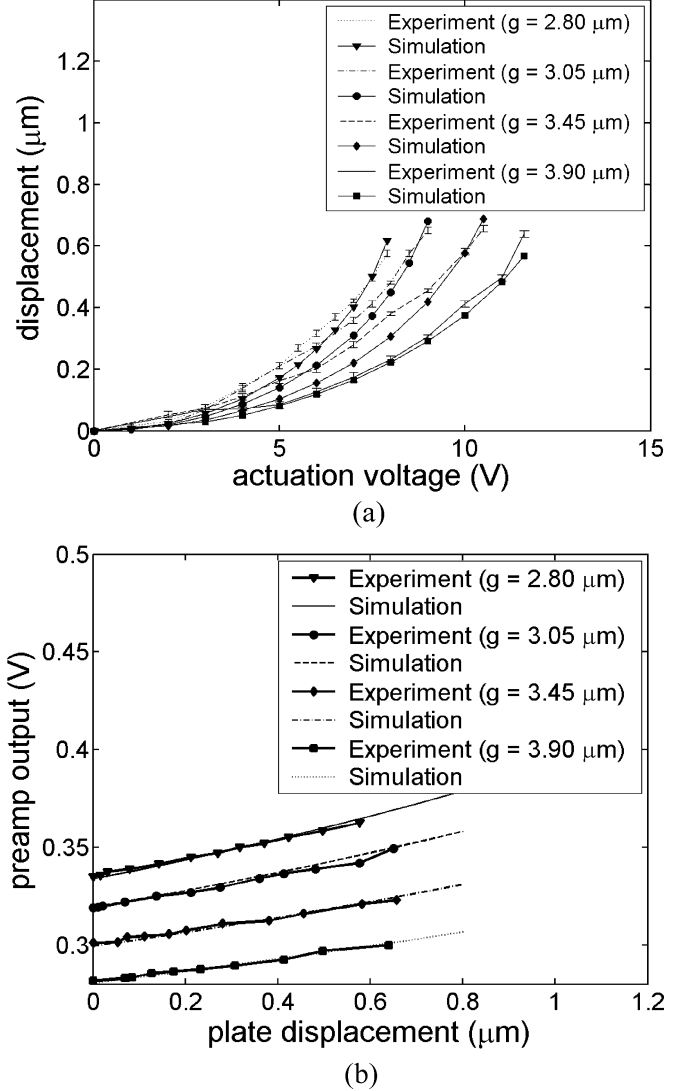


(a)



(b)

Fig. 11. (a) Measured displacement-voltage characteristic extracts actuator spring constant at 0.17 N/m. (b) Measured pre-amp output with respect to actuator displacement extracts total pre-amp input capacitance at 333 fF.

motion with a measuring error around 10 nm due to the fringe contrast. A dc voltage was incrementally applied to the actuator, and an ac modulation voltage of 1 V at 4.5 MHz was applied to the top electrode for capacitive sensing. Actuator snap-in was prevented with the measurements performed within the pull-in limit. The measured and simulated displacement-voltage characteristic shown in Fig. 11(a) leads to an extracted actuator spring constant of 0.17 N/m. The preamp input capacitance was 333 fF, as extracted from the measured pre-amp output amplitude with respect to the actuator displacement in Fig. 11(b).

The actuator resonant frequency was measured electronically by an Agilent 4395A spectrum analyzer, which detected the readout signal from the demodulator to construct the actuator frequency response. The resonant frequency decreases as a result of the spring-softening effect from the increasing dc bias. Both experimental and NODAS simulation results are shown in Fig. 12(a), in which the actuator resonant frequency is found at 12.4 kHz. From the resonant peak of the measured frequency response, the effective damping ratio shown in Fig. 12(b) is calculated in between 0.55 to 0.35 for gaps between 2.3 to 2.65 $\mu$m.
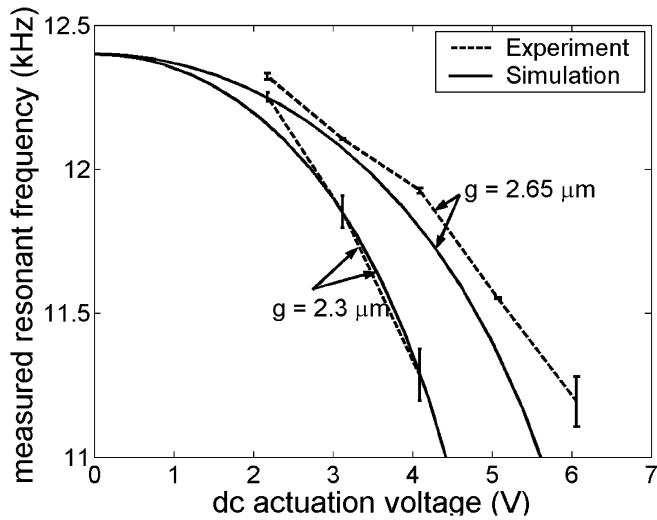
(a)
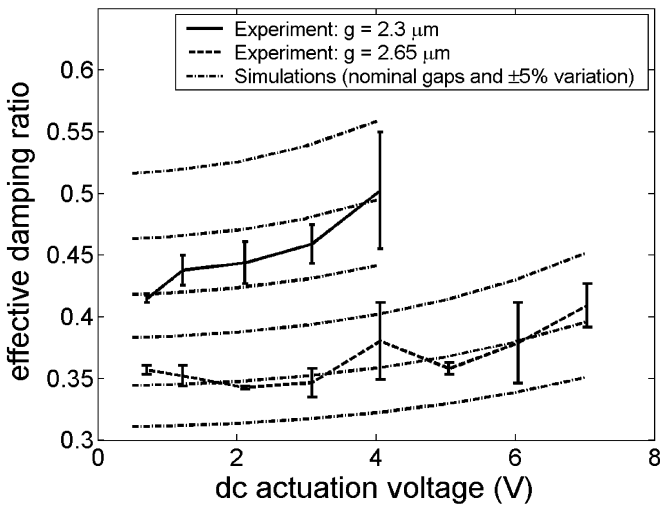


(b)

Fig. 12.   (a) Measured actuator resonant frequency with respect to applied dc actuation voltage. Increased dc bias enhances spring-softening effect, as evidenced by the resonant frequency drop. (b) Measured effective damping ratio with respect to applied dc actuation voltage. Effective damping ratio increases as the gap closes on with increasing dc bias.

The minimum detectable displacement was determined by the pre-amp noise and the closed-loop bandwidth. We measured the minimum input-referred noise voltage by applying a 200 mV ac voltage at 2 kHz to the actuator, and measuring the pre-amp output at a 1-Hz bandwidth. The measured input-referred voltage at a 1-Hz bandwidth is plotted as a function of gap separation in Fig. 13, which illustrates a minimum input-referred noise voltage of $1.4\,\mu\text{V}/\sqrt{\text{Hz}}$ at a gap around 5.7 $\mu$m. By calculation, the minimum input-referred noise voltage is equivalent to a minimum input-referred noise capacitance change and a minimum input-referred noise displacement of $0.5\,\text{aF}/\sqrt{\text{Hz}}$ and $0.33\,\text{nm}/\sqrt{\text{Hz}}$, respectively.

## VII. Closed-Loop Step Response

The controller used in the closed-loop experiments was $C(s) = 24.3$, and the prefilter design was $F(s) = 1/$
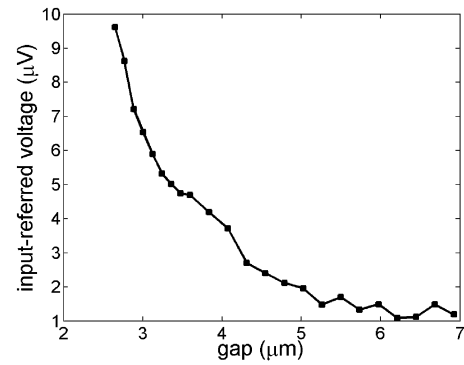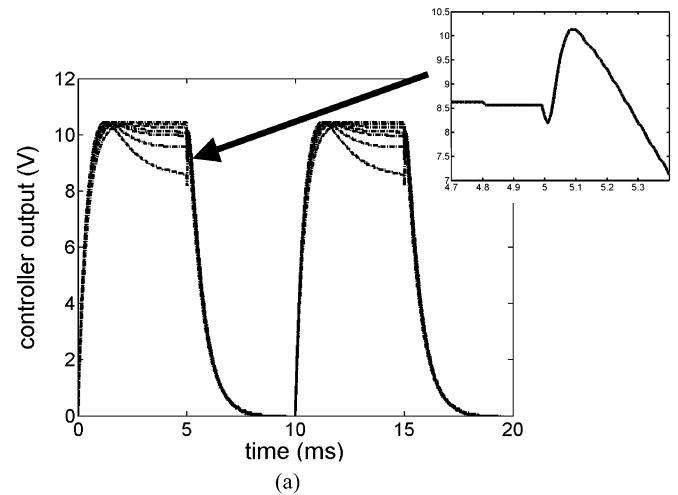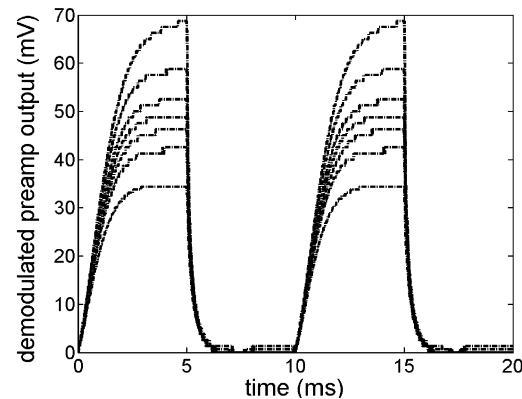


Fig. 13.   Measured input-referred voltage at 1 Hz resolution bandwidth versus gap separation.



(a)



(b)

Fig. 14.   (a) Measured controller waveforms when the actuator moves into snap-in region and beyond. The inset illustrates its waveform when the input command turns from high to low. (b) Measured demodulated pre-amp output waveforms.

$(s/1800 + 1)$. The controller gain is higher than the previously designed $k_p = 16$ to compensate for the measured pre-amp gain reduction of 2.2 dB at the modulation frequency of 4.5 MHz, and the reduced damping due to plate tilt. The applied input command for closed-loop measurement was a square-wave voltage at 100 Hz with the minimum set at zero. A series of controller output waveforms was measured when the actuator moved into the snap-in region and beyond, as shown in Fig. 14(a). Decrease of controller output after the pull-in volt
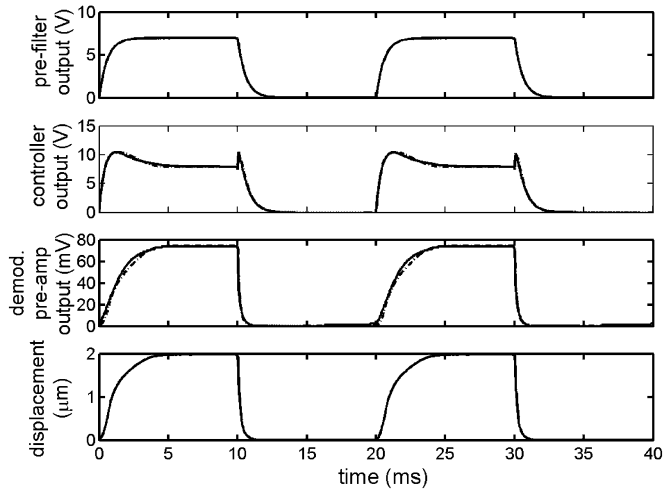
Fig. 15. Measured waveforms (dash lines) and simulated waveforms (solid lines) of prefilter output, controller output, demodulated pre-amp output, and plate displacement to a 50-Hz square-wave input-command voltage.
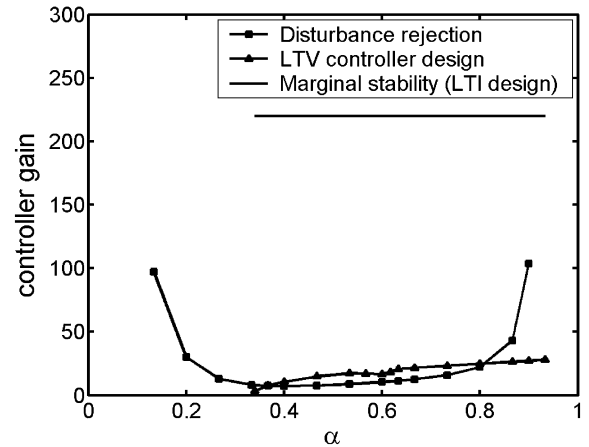


Fig. 16. The minimum controller gain plotted as a function of normalized displacement for input disturbance rejection. Also plotted is the optimal linear time-varying design from Fig. 9(d), and the maximum applied gain to maintain a marginal system stability.

age (10.44 V) reduces the stored charge on the plates to stabilize the actuator beyond the pull-in limit. As the input command changes from high to low, the controller output first decreases, and then increases to maintain stability as the actuator retracts back to the rest position, as shown by the inset in Fig. 14(a). Measured demodulated pre-amp output waveforms are shown in Fig. 14(b), which illustrate an increase in rise time as the input-command magnitude increases, primarily because of the increase of damping.

Measured controller output waveforms and demodulated pre-amp output waveforms are compared with the closed-loop NODAS simulations, in which we model the parallel-plate actuator using 3-D elastic beams, 3-D elastic plates, squeeze-film damping elements, and electrostatic gap models. The measured and simulated prefilter output, controller output, demodulated pre-amp output, and plate displacement to the largest input command at 50 Hz are plotted in Fig. 15 with very good agreement. A maximum displacement of 2 $\mu$m, equivalent to 60% of the gap ($g = 3.3\ \mu$m) is illustrated. Fall time of the plate displacement is significantly shorter than its rise time because the actuator dynamics is different in the falling period, in which the spring restoring force, not the electrostatic force, provides acceleration for the actuator when it retracts back to the rest position. Also the experienced damping force reduces as the actuator moves away from the top electrode.

## VIII. DISCUSSION AND CONCLUSION

We have successfully demonstrated a maximum travel range of 60% of the gap by using the closed-loop voltage control approach. The failure of control loop beyond 60% of the gap is mainly contributed to the loss of phase margin. Insufficient phase margin can lead to output oscillation. As for our case, system instability is likely to happen with the actuator dynamics being different in the forward and backward directions during oscillation. In other words, the same controller may induce instability when the actuator moves away from the opposing electrode. This is why sufficient phase margin is given in our design

to produce an overdamped response. Phase margin decreases with respect to the increasing spring-softening effect and the reduced damping coefficient resulted from plate tilt. Tilted plates result in 30% more of the spring-softening effect than that of the parallel-plate case at 60% of the gap, thereby reducing the phase margin by about 10°. The majority of the phase-margin loss is due to the decrease of damping coefficient. The damping ratio of the tilted plates at 60% of the gap is only 20% to 30% of that for the parallel plates, thereby reducing the phase margin by about 30°.

The linearization technique used for analysis and design of the controller excludes the effects of initial conditions (i.e., plate velocity and acceleration) and perturbation of plate displacement. Those effects are crucial in design of nonlinear control systems, and can contribute to the failure of servo designed by the linearization technique. Therefore, to enhance the robust stability, they are modeled as an equivalent disturbance force injected into the input of the linearized mass-damper-spring model, and formulated as a disturbance-rejection problem within the feedback framework. Disturbance rejection often requires more gain and/or bandwidth from the controller in addition to realizing the required stability margins for system stability. Due to the highly unstable pole at very small gaps, the required controller gain for disturbance rejection can increase drastically with respect to the plate displacement. As shown in Fig. 16, the required controller gain is close to 100 for the plate displacement up to 90% of the initial gap to ensure robust stability against disturbances, whereas the current controller gain is insufficient with the value about one-fifth of the required gain. To compare the gain requirement from the previous stability analysis, also shown on the plot are the optimal LTV design from Fig. 9(d), and the maximum LTI controller gain $k_p = 220$ to maintain a marginal system stability (phase margin = 0°). If a controller gain $k_p = 80$ is used for disturbance rejection, the minimum phase margin can be reduced to 20°, which is much less than the common 60° phase margin for system stabilization. From the plot we can conclude that it is difficult to simultaneously satisfy the phase-margin and the

disturbance-rejection requirements for highly unstable plants at displacements beyond 80% of the initial gap. Also note that the required high gain for disturbance rejection at small displacements on the plot is expected because the output displacement does not behave quasi-statically due to the initial acceleration. Therefore the controller must have more gain to force the output back to the quasi-static trajectory. However system stability in the small-displacement region is not affected because the actuator is in the stable regime, and required controller gain for disturbance rejection meets our LTI design before reaching into the unstable regime.

For the proposed probe-based microdisk drive, a displacement up to 83% of the initial gap is preferred to accommodate a tip height of 500 nm. Given the achieved 60% travel range, increase of a total tip height to 1.2 $\mu$m has been suggested to reduce the required plate displacement by additional thin-film deposition underneath the tip. Future fabrication of the tip actuator array can benefit from the use of the CMOS-MEMS process for its convenient high-speed circuit integration and existing interconnect to route signals in the array.

Nonlinearities of the actuator and capacitive sensor are successfully resolved with a LTI proportional-gain controller. Integral control can be included in the future to eliminate the steady-state error from use of a simple proportional-gain controller. However a very low-frequency zero has to be included in the controller to compensate for the 90° phase lag of an integrator. The selection of the two degree-of-freedom control system is crucial as it decouples the design processes for closed-loop stability and output tracking. For most stable plants, a single controller may simultaneously handle both requirements because the classical control theory states that the overshoot in the output can be eliminated by designing with a 60° phase margin; however this does not hold true for plants with unstable poles, so there is no guarantee that both requirements can be satisfied under such circumstances. To resolve this issue and for efficient design of open-loop bandwidth, we recognize that output tracking should be realized by open-loop compensation, then the closed-loop feedback can focus on securing robust stability only.

In the context of reduced damping due to plate tilt, the dilemma for design of open-loop bandwidth lies in the difficulty to obtain adequate phase margin without amplification of the sensor noise. The implemented loop bandwidth is however already limited by the use of a low-pass filter after the demodulator, thereby reducing the attainable phase margin. From the controller design standpoint, use of a LTI controller facilitates the implementation but is less versatile in terms of bandwidth efficiency and attainable gain and phase margins than other alternatives, such as a nonlinear controller and a LTV controller. Those types of controllers remain interesting research topics for the future.

## REFERENCES

[1] X. T. Wu, R. A. Brown, S. Mathews, and K. R. Farmer, "Extending the travel range of electrostatic micro-mirrors using insulator coated electrodes," in *Proc. IEEE/LEOS Int. Conf. Opt. MEMS 2000*, Kauai, HI, 2000, pp. 151–152.

[2] C. Cabuz, "Dielectric related effects in micromachined electrostatic actuators," in *Proc. Conf. Electrical Insulation and Dielectric Phenomena*, Austin, TX, Oct. 17–20, 1999, pp. 327–332.

[3] R. Legtenberg, J. Gilbert, S. D. Senturia, and M. Elwenspoek, "Electrostatic curved electrode actuators," *J. Microelectromech. Syst.*, vol. 6, pp. 257–265, Sept. 1997.

[4] E. S. Hung and S. D. Senturia, "Extending the travel range of analog-tuned electrostatic actuators," *J. Microelectromech. Syst.*, vol. 8, pp. 497–505, Dec. 1999.

[5] E. K. Chan and R. W. Dutton, "Electrostatic micromechanical actuator with extended range of travel," *J. Microelectromech. Syst.*, vol. 9, pp. 321–328, Sept. 2000.

[6] J. I. Seeger and S. B. Crary, "Stabilization of electrostatically actuated mechanical devices," in *Proc. Int. Conf. on Solid-State Sensors and Actuators (Transducers '97)*, Chicago, IL, June 16–19, 1997, pp. 1133–1136.

[7] L. M. Castañer and S. D. Senturia, "Speed-energy optimization of electrostatic actuators based on pull-in," *J. Microelectromech. Syst.*, vol. 8, pp. 290–298, Sept. 1999.

[8] J. I. Seeger and B. E. Boser, "Dynamics and control of parallel-plate actuators beyond the electrostatic instability," in *Proc. Int. Conf. on Solid-State Sensors and Actuators (Transducers '99)*, Sendai, Japan, June 7–10, 1999, pp. 474–477.

[9] R. N. Guardia, R. Aigner, W. Nessler, M. Handtmann, and L. M. Castañer, "Control positioning of torsional electrostatic actuators by current driving," in *Proc. 3rd Int. Euroconf. on Advanced Semiconductor Devices and Microsystems*, Sinolenice Castle, Slovakia, 2000, pp. 91–94.

[10] P. B. Chu and K. S. Pister, "Analysis of closed-loop control of parallel-plate electrostatic microgrippers," in *Proc. Int. Conf. Robotics Automation*, San Diego, CA, May 8–13, 1994, pp. 820–825.

[11] D. F. Guillou, "Control of MEMS Electrostatic Parallel-Plate Actuators," Ph.D. dissertation, Dept. Elec. Comput. Eng., Carnegie Mellon Univ., Pittsburgh, PA, 2002.

[12] L. R. Carley, J. A. Bain, G. K. Fedder, D. W. Greve, D. F. Guillou, M. S.-C. Lu, T. Mukherjee, S. Santhanam, L. Abelmann, and S. Min, "Single-chip computers with microelectromechanical system-based magnetic memory," *J. Appl. Phys.*, pt. 1–3, vol. 87, no. 9, pp. 6680–6685, 2000.

[13] A. M. Lyapunov, "The general problem of motion stability," in *Ann. Math. Study*. Princeton, NJ: Princeton University, 1949.

[14] I. Fantoni, R. Lorano, and M. W. Spong, "Energy based control of the pendubot," *IEEE Trans. Automat. Contr.*, vol. 45, pp. 725–729, Apr. 2000.

[15] I. M. Horowitz and M. Sidi, "Synthesis of feedback systems with large plant ignorance for prescribed time-domain tolerances," *Int. J. Control*, vol. 16, no. 2, pp. 287–309, 1972.

[16] G. K. Fedder, S. Santhanam, M. L. Reed, S. C. Eagle, D. F. Guillou, M. Lu, and L. R. Carley, "Laminated high-aspect-ratio microstructures in a conventional CMOS process," *Sens. Actuators A, Phys.*, vol. A57, no. 2, pp. 103–110, 1997.

[17] "Robert Bosch GmbH," U.S. Patent 4 784 720 and 4 855 017.

[18] J. J. Blech, "On isothermal squeeze films," *J. Lubrication Tech.*, vol. 105, pp. 615–620, 1983.

[19] T. Veijola, H. Kuisma, J. Lahdenperä, and T. Ryhänen, "Equivalent-circuit model of the squeezed gas film in a silicon accelerometer," *Sens. Actuators A, Phys.*, vol. A48, pp. 239–248, 1995.

[20] S. Vemuri, G. K. Fedder, and T. Mukherjee, "Low-order squeeze film model of simulation of MEMS devices," in *Proc. Int. Conf. on Modeling and Simulation of Microsystems*, San Diego, CA, March 27–29, 2000, pp. 205–208.

[21] *ABAQUS Manual, Version 6.2*, Hibbitt, Karlsson, and Sorensen, Inc., 2001.

[22] P. R. Gray and R. G. Meyer, *Analysis and Design of Analog Integrated Circuits*, 3rd ed. New York: Wiley, 1993.

[23] G. K. Fedder and Q. Jing, "A hierarchical circuit-level design methodology for microelectromechanical systems," *IEEE Trans. Circuits Syst. II*, vol. 46, no. 10, pp. 1309–1315, 1999.

[24] M. S.-C. Lu, "Parallel-Plate Micro Servo for Probe-Based Data Storage," Ph.D. dissertation, Dep. Elec. Comput. Eng., Carnegie Mellon Univ., Pittsburgh, PA, 2002.

[25] I. M. Horowitz, *Synthesis of Feedback Systems*. New York: Academic, 1965.

[26] D. P. Looze and J. S. Freudenberg, "Limitations of feedback properties imposed by open-loop right half plane poles," *IEEE Trans. Automat. Contr.*, vol. 36, no. 6, pp. 736–739, June 1991.

[27] H. Nyquist, "Regeneration theory," *Bell Syst. Tech. J.*, vol. 11, pp. 126–147, 1932.

[28] *Maxwell 2D Field Simulator: User's Reference, Version 2.5.55*, Ansoft Corporation, Pittsburgh, PA, 2001.

**Michael S.-C. Lu** was born in Taipei, Taiwan, R.O.C., in 1968. He received the B.S. and M.S. degrees in power mechanical engineering from National Tsing Hua University, Hsinchu, Taiwan, in 1991 and 1993, respectively. In 2002, he received the Ph.D. degree in electrical engineering from Carnegie Mellon University, Pittsburgh, PA.

Since August 2002, he has been an Assistant Professor with the Department of the Electrical Engineering and the Electronics Institute at National Tsing Hua University, Taiwan. His research interests include integrated CMOS-micromachined sensors and actuators, probe-based data storage and manipulation, and control systems.

**Gary K. Fedder** (S'93–M'95–SM'98) received the B.S. and M.S. degrees in electrical engineering from the Massachusetts Institute of Technology (MIT), Cambridge, in 1982 and 1984, respectively. In 1994, he received the Ph.D. degree from University of California at Berkeley, where his research resulted in the first demonstration of multimode control of a underdamped surface-micromachined inertial device.

From 1984 to 1989, he worked at the Hewlett-Packard Company on circuit design and printed-circuit modeling. He is a Professor at Carnegie Mellon University, Pittsburgh, PA, holding a joint appointment with the Department of Electrical and Computer Engineering and The Robotics Institute. He has contributed to over 100 research publications and several patents in the MEMS area. His research interests include microsensor and microactuator design and modeling, integrated MEMS manufactured in CMOS processes, and structured design methodologies for MEMS.

Dr. Fedder received the 1993 AIME Electronic Materials Society Ross Tucker Award, the 1996 Carnegie Institute of Technology G. T. Ladd Award, and the 1996 NSF CAREER Award. Currently, he serves as a Subject Editor for the IEEE/ASME JOURNAL OF MICROELECTROMECHANICAL SYSTEMS, on the editorial board of the *IoP Journal of Micromechanics and Microengineering* and as co-editor of the Wiley-VCH Advanced Micro and Nanosystems book series.